*Atmospheric Science Letters*

RMetS Royal Meteorological Society

RESEARCH ARTICLE OPEN ACCESS

# Three-Year Characterization of Boundary Layer Dynamics From GNSS Zenith Wet Delay Spectral Analysis

Gaël Kermarrec[1] | Xavier Calbet[2] | Zhiguo Deng[3]

[1]Institut für Meteorologie Und Klimatologie (IMUK)|, Leibniz Universität Hannover, Hannover, Germany | [2]Agencia Estatal de Meteorología (AEMET), Madrid, Spain | [3]Helmholtz Centre Potsdam, GFZ German Research Centre for Geosciences, Potsdam, Germany

**Correspondence:** Gaël Kermarrec (kermarrec@meteo.uni-hannover.de)

**Received:** 3 December 2025 | **Revised:** 5 May 2026 | **Accepted:** 8 May 2026

**Keywords:** anisotropy | boundary layer turbulence | climatology | GNSS meteorology | spectral analysis | zenith wet delay

## ABSTRACT

Continuous monitoring of boundary layer turbulence remains a challenge due to sparse conventional instrumentation. Here we suggest that spectral analysis of Global Navigation Satellite System (GNSS) zenith wet delay (ZWD) fluctuations yields physically meaningful diagnostics of boundary layer state. From 3 years of co-located GNSS and Doppler lidar observations (January 2022–December 2024, $N = 52{,}608$) at Payerne, Switzerland, we extract the variance $\sigma^2$, a measure of integrated water vapor turbulence intensity, and the cutoff frequency $\alpha$, which marks the spectral extent of turbulent mixing. Annual harmonic analysis reveals that $\alpha$ captures 54% of its variance through the seasonal cycle ($R^2 = 0.54$, peak in January), while $\sigma^2$ peaks in August ($R^2 = 0.21$). The inverse $\alpha$–$\sigma^2$ coupling ($r = -0.57$) tightens to $r = -0.82$ under summer convective conditions, consistent with regime-dependent physical correspondence. Cross-instrument comparison with Doppler lidar turbulent kinetic energy (TKE) integrated over 100–550 m is compatible with the fundamental vertical sampling mismatch between troposphere-weighted GNSS and profile-limited lidar measurements. These results establish GNSS networks as a globally available sensing system for boundary layer turbulence monitoring.

## 1 | Introduction

Atmospheric turbulence in the planetary boundary layer (PBL) governs the vertical transport of heat, moisture, and momentum between the Earth's surface and the free troposphere (Stull 1988). The intensity and spatial structure of turbulent mixing vary dramatically with season in response to the annual cycle of solar forcing that modulates surface heating and atmospheric stability. During summer, strong insolation drives convective boundary layers that at midlatitude continental sites extend to 2–3 km depth, sustain vigorous vertical exchange, and homogenize potential temperature and mixing ratio throughout the mixed layer. In contrast, winter conditions favor stable stratification with persistent temperature inversions that suppress vertical mixing and confine turbulent motions to shallow surface-based layers (Kaimal et al. 1976).

Understanding this seasonal variability is essential across multiple domains. Weather prediction relies critically on accurate representation of boundary layer processes that control surface fluxes and cloud formation. Air quality forecasting requires knowledge of atmospheric dispersion capacity, which varies inversely with boundary layer stability—stable conditions trap pollutants near the surface while convective mixing dilutes them through deeper layers. Wind energy production depends on both turbulence intensity, which modulates power output fluctuations, and wind shear profiles shaped by stability. Climate modeling must accurately represent the boundary layer's role in surface-atmosphere coupling to reproduce regional patterns (Lothon et al. 2014).

Traditional observing systems provide valuable but incomplete characterization of boundary layer turbulence. Radiosondes, launched twice daily, offer high-resolution profiles but miss

critical diurnal evolution. Wind profilers and Doppler lidars provide continuous coverage but are spatially sparse. Surface flux towers sample only the surface layer, missing mixed-layer turbulence (Emeis 2008). This spatial sparsity fundamentally limits regional characterization of turbulence climatology.

Global Navigation Satellite System (GNSS) networks offer an attractive complement. With over 10,000 continuously operating stations worldwide, GNSS provides unprecedented spatial coverage across diverse climate zones and terrain types. These receivers routinely estimate zenith wet delay (ZWD), the propagation delay caused by atmospheric water vapor (Bevis et al. 1992). While GNSS-derived water vapor is established in operational meteorology for data assimilation and nowcasting (Guerova et al. 2016), the potential of high-frequency ZWD fluctuations to characterize turbulence has received limited attention.

Recent theoretical work demonstrated that ZWD fluctuations exhibit spectral characteristics consistent with turbulent cascades. Under the Taylor frozen-flow hypothesis (Taylor 1938), which relates spatial and temporal fluctuations through mean advection velocity, integrated water vapor follows a $-8/3$ power law in the power spectral density. This scaling is analogous to the Kolmogorov $-5/3$ law modified for line-of-sight integration through turbulent media (Tatarski 1961). Fitting a von Kármán spectrum (Lilly 2017) yields two parameters: variance $\sigma^2$, a measure of turbulence intensity, and cutoff frequency $\alpha$, which delineates the inertial subrange boundary. A preliminary study demonstrated the feasibility of this approach across multiple climate zones using 1 year of observations (Kermarrec et al. 2025), but validation against independent turbulence measurements over climatological timescales remains lacking.

This study presents the first three-year analysis correlating GNSS ZWD spectral parameters with independent turbulence measurements from Doppler lidar. Using three complete annual cycles of continuous observations at Payerne, Switzerland (January 2022–December 2024), we quantify correlations between $\alpha$, $\sigma^2$, and vertically integrated TKE, and introduce annual harmonic analysis to objectively characterize the seasonal cycle. We further introduce an anisotropy index from velocity variance ratios that offers additional regime discrimination. Diurnal case studies in Appendix A complement the seasonal analysis with evidence of physically meaningful within-day coupling. Our results indicate that existing GNSS networks can serve as globally distributed observing systems for atmospheric mixing monitoring.

## 2 | Data and Methods

This section describes the observational site and instrumentation, data quality control procedures, vertical integration of lidar profiles, spectral parameter estimation from ZWD time series, and the anisotropy index used for regime discrimination.

### 2.1 | Observational Site and Instrumentation

Observations were obtained from the MeteoSwiss Aerological Station at Payerne, Switzerland (46.82° N, 6.94° E, 491 m ASL), a certified GRUAN reference site with comprehensive atmospheric profiling capabilities (Navas-Guzmán et al. 2019). The station lies in the Swiss Plateau; relatively flat terrain minimizes complications from terrain-induced circulations that would complicate turbulence interpretation.

The station hosts co-located GNSS receivers, a Windcube 200 s Doppler wind lidar, and a ceilometer, so that all observations sample the same atmospheric column. ZWD retrievals were computed using EPOS.P8 software (Neumayer et al. 2024) at 30-s resolution, processing dual-frequency GPS/GLONASS observations in precise point positioning mode with final precise orbits, absolute antenna corrections, and Vienna Mapping Functions. The raw dataset comprises approximately 3.15 million individual ZWD estimates.

The Windcube 200 s Doppler lidar operates at 1.54 μm wavelength, detecting aerosol backscatter to retrieve wind vectors. The instrument alternates between two operational modes in a scheduled cycle: conical velocity-azimuth display (VAD) scans at multiple azimuth angles for three-dimensional wind vector retrieval, and high-resolution vertical stare mode (90° elevation) for direct measurement of vertical velocity. Horizontal velocity variances ($\overline{u'^2}$, $\overline{v'^2}$) are obtained from the VAD analysis, while vertical velocity variance ($\overline{w'^2}$) is derived from the vertical stare measurements. This component—most sensitive to scanning strategy (Newman et al. 2016; Bonin et al. 2017)—is thus measured directly without assumptions about horizontal homogeneity. TKE is computed as $\frac{1}{2}\left(\overline{u'^2}+\overline{v'^2}+\overline{w'^2}\right)$ over 30-min windows at 50 m vertical resolution.

### 2.2 | Data Quality Control

The analysis spans the full three-year period January 2022–December 2024 ($N = 52{,}608$ half-hourly epochs, three complete annual cycles with > 95% coverage).

Outlier removal is critical for correlation analysis, as sporadic measurement spikes in lidar-derived quantities can dominate statistics and mask genuine atmospheric signals. We employed a four-pass algorithm that combines complementary approaches for robust detection (Leys et al. 2013): (1) median-based detection with threshold factors 1.2–2.0 depending on variable sensitivity, chosen because median estimators resist contamination by the very outliers being detected; (2) quantile clipping at 3rd/97th percentiles to remove extreme values that survived initial filtering; (3) a 21-point moving median filter to smooth residual isolated spikes while retaining synoptic variability; (4) secondary outlier detection with relaxed thresholds to catch remaining artifacts. This iterative approach proved necessary given the heterogeneous noise characteristics across variables—TKE and wind variances exhibited frequent spikes from lidar signal dropouts, while $\alpha$ and $\sigma^2$ behaved more smoothly. Missing values were linearly interpolated.

Temporal smoothing combined Savitzky–Golay filtering (Savitzky and Golay 1964) (144-point window, 3 days) with moving average (96-point, 2 days), for an effective 5-day smoothing that emphasizes synoptic-to-seasonal variability and attenuates diurnal cycles and high-frequency noise.

### 2.3 | Vertical Integration

Lidar profiles were vertically integrated from 100 to 550 m altitude (10 levels at 50 m spacing). The lower limit avoids surface-layer complications and instrument blind zone; the upper limit stays within typical mixed-layer depths and maintains adequate signal quality (data gaps, outliers). Integrated TKE was computed via trapezoidal integration:

$$\mathrm{TKE}_{\mathrm{int}} = \int_{100}^{550} \mathrm{TKE}(z)\,dz. \tag{1}$$

Similarly, velocity variances were integrated for zonal ($u'$), meridional ($v'$), and vertical ($w'$) components.

### 2.4 | Spectral Parameter Estimation

Power spectral density of detrended ZWD was estimated using the Thomson multitaper method (Thomson 1982) with time-bandwidth product NW = 4 and K = 7 tapers, which yields robust estimates with reduced variance. We fit a Matérn spectrum representing von Kármán turbulence:

$$W_x(\omega) = \frac{\sigma^2 \alpha^{5/3}}{c_\alpha \left(\omega^2 + \alpha^2\right)^{4/3}}, \tag{2}$$

where $\sigma^2$ is process variance ($\mathrm{m}^2$), $\alpha$ the cutoff frequency ($\mathrm{s}^{-1}$) marking the transition between energy-containing and inertial subranges, and $c_\alpha \approx 1.868$ a normalization constant. Parameter estimation employs debiased Whittle likelihood (Sykulski et al. 2019) with spectral slope fixed at $-8/3$ as predicted by theory for integrated scalar fields.

### 2.5 | Anisotropy Index

To characterize turbulence directional structure and discriminate regimes, we computed:

$$A = \frac{\int_{100}^{550} \overline{w'^2}(z)\,dz}{\int_{100}^{550} \overline{u'^2}(z)\,dz}. \tag{3}$$

Values $A > 1$ indicate vertical dominance characteristic of buoyancy-driven convection; $A < 1$ indicates horizontal dominance from shear or stable conditions. This ratio-of-integrals formulation proved most robust among tested alternatives, including the ratio at fixed height (300 m), the profile maximum, and the $w'^2 / v'^2$ ratio.

## 3 | Results

### 3.1 | Three-Year Time Series

Figure 1a presents the three-year time series (January 2022–December 2024) of GNSS-derived spectral parameters alongside integrated TKE and cloud cover. Both $\alpha$ and $\sigma^2$ exhibit pronounced seasonal cycles persisting with remarkable consistency across all three annual cycles.

The variance $\sigma^2$ displays clear summer maxima (June–August) and winter minima (December–February), with peak-to-trough ratios exceeding two. Summer values typically range from 2.5 to $3.0 \times 10^{-3}\,\mathrm{m}^2$, while winter values fall to $1.5\text{–}2.0 \times 10^{-3}\,\mathrm{m}^2$. This pattern traces the seasonal modulation of convective mixing: summer solar heating drives intense surface-based convection whose buoyant thermals carry water vapor through substantial atmospheric depth. Deep convective boundary layers reaching 2–3 km during summer afternoons sustain moisture exchange over the full mixed-layer column. In contrast, winter radiative cooling establishes persistent temperature inversions that suppress vertical mixing and reduce ZWD variability.

The cutoff frequency $\alpha$ exhibits inverse seasonality: systematically higher winter values (0.035–0.045 $\mathrm{s}^{-1}$) and lower summer values (0.020–0.030 $\mathrm{s}^{-1}$). Physically, $\alpha$ represents the frequency below which turbulent fluctuations transition from the inertial subrange to larger outer-scale motions controlled by boundary layer depth. During convection, deep boundary layers with energetic thermals push the inertial range toward lower frequencies, pulling $\alpha$ down. Large eddies with horizontal scales of hundreds of meters produce fluctuations with periods of 10–30 min. Winter stable conditions confine turbulence to shallow layers, shifting cutoff to higher frequencies characteristic of smaller structures.

Integrated TKE from lidar corroborates these patterns, with summer maxima coincident with peak $\sigma^2$. Cloud cover exhibits more complex variability, i.e., autumn/winter higher fractions associated with stable stratiform decks.

Figure 1b presents integrated velocity variances. Vertical fluctuations ($\int w'^2 dz$) consistently exceed horizontal components, with clear summer maxima and values in the range 1000–4000 $\mathrm{m}^3\,\mathrm{s}^{-2}$. Zonal variance ($\int u'^2 dz$) follows a similar seasonal pattern but with smaller amplitude (5–25 $\mathrm{m}^3\,\mathrm{s}^{-2}$). Meridional variance ($\int v'^2 dz$) remains notably weak, which points to a boundary layer dominated by convective vertical motions and zonal shear at Payerne. This preponderance of vertical motions is consistent with buoyancy-driven processes as the primary control on observed seasonal variability.

### 3.2 | Correlation Analysis

Table 1 summarizes Pearson correlations between all parameters over the full three-year record. The $\alpha$–$\sigma^2$ coupling ($r = -0.57$) attests to the internal consistency of the spectral model: both parameters are co-estimated from the von Kármán fit, and their inverse relationship implies that the model captures complementary aspects of boundary layer state. Cross-instrument validation rests on the $\sigma^2$–TKE ($r = +0.20$) and $\alpha$–TKE ($r = -0.29$) correlations, which constitute independent evidence that GNSS-derived parameters respond to boundary layer turbulence. The moderate magnitudes of these cross-instrument correlations are consistent with the vertical sampling mismatch discussed in Section 4.

The $\alpha$–$\sigma^2$ coupling exhibits pronounced regime dependence: $r = -0.82$ during summer (JJA) when convection dominates, weakening to $r = -0.55$ in winter (DJF) and $r = -0.40$ in spring (MAM). This seasonal modulation rules out a statistical

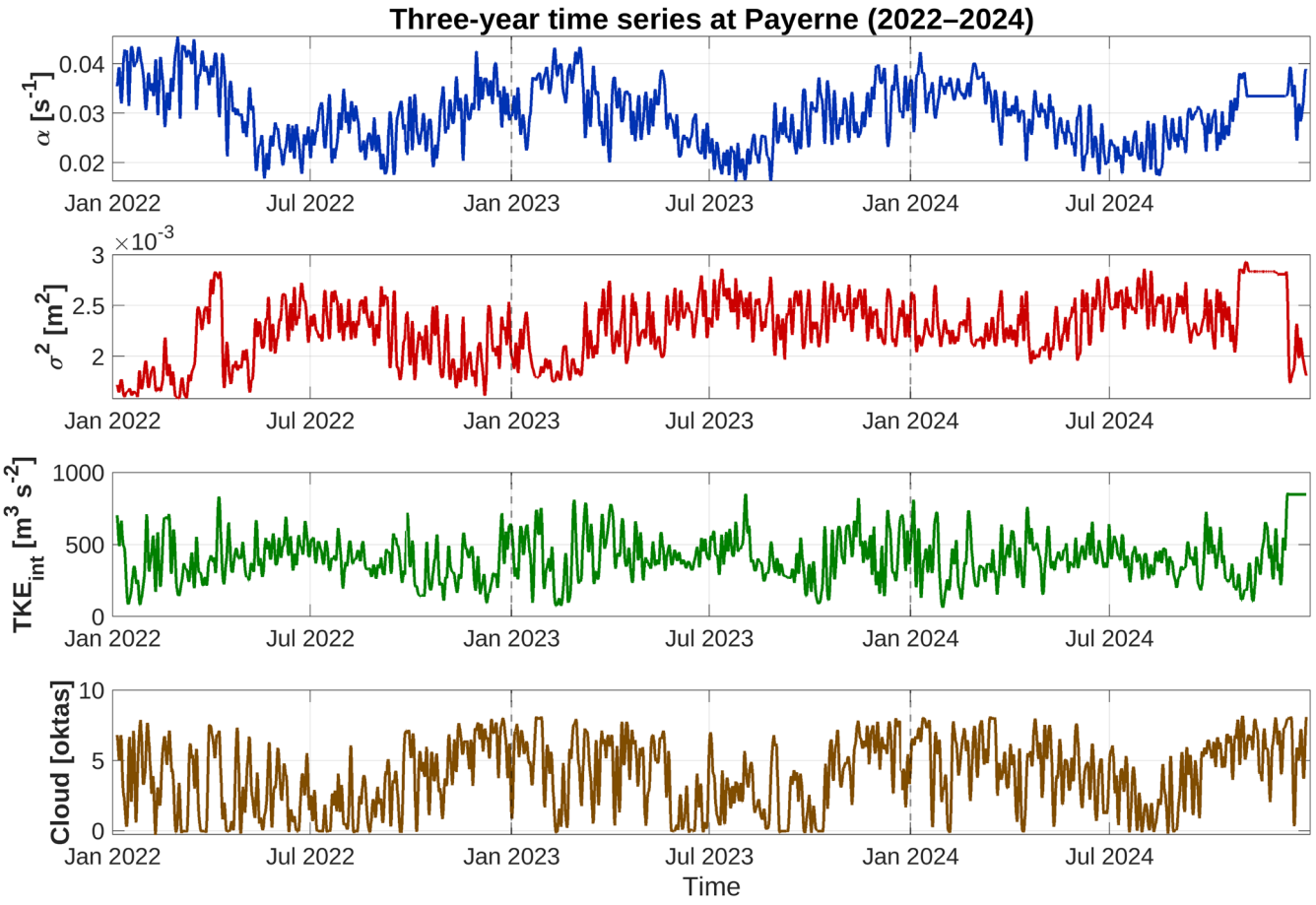


(a) GNSS-derived spectral parameters ($\alpha$, $\sigma^2$), integrated TKE (100–550 m), and cloud cover fraction.

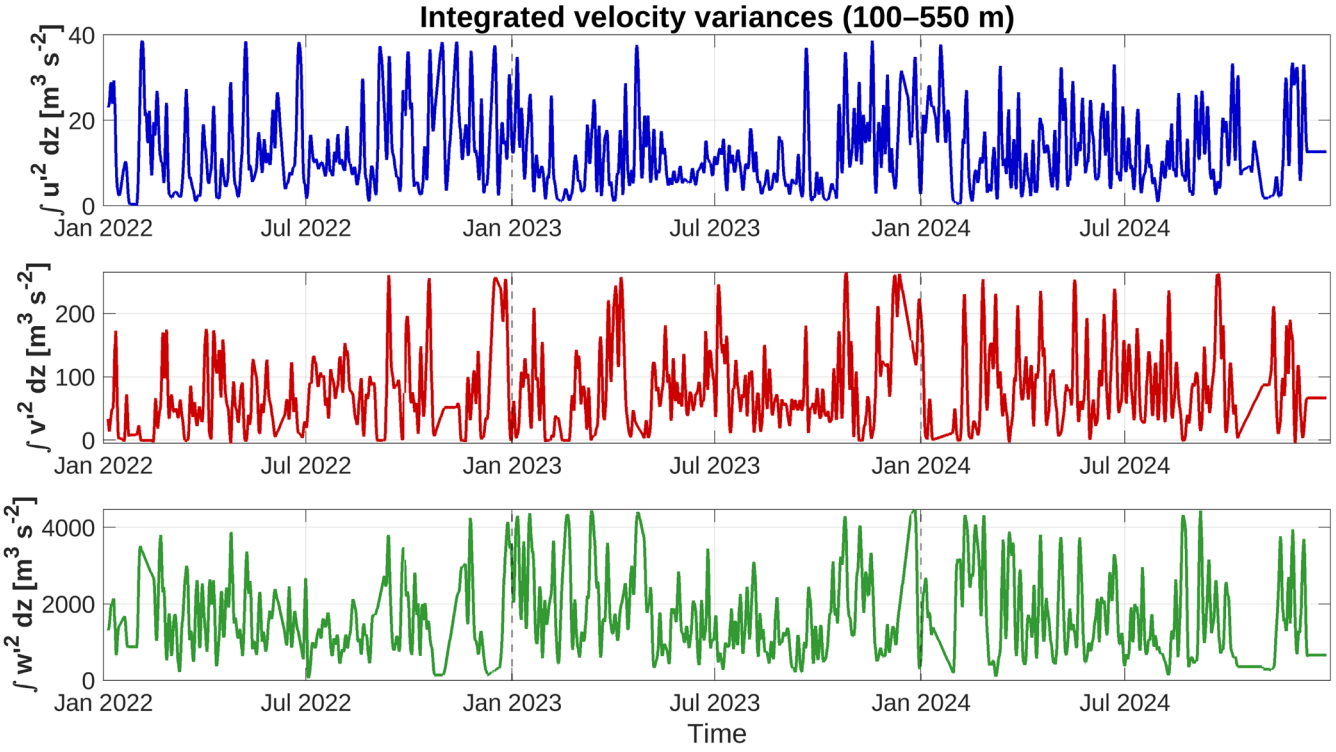


(b) Vertically integrated wind velocity variances: zonal ($\int u'^2 dz$), meridional ($\int v'^2 dz$), and vertical ($\int w'^2 dz$).

**FIGURE 1** | Time series (January 2022–December 2024) at Payerne, Switzerland. Vertical dashed lines indicate year boundaries.

**TABLE 1** | Correlation matrix for GNSS and lidar parameters (January 2022–December 2024, $N = 52{,}608$).

| | $\sigma^2$ | TKE | Cloud | Anisotropy $A$ |
|---|---|---|---|---|
| $\alpha$ | –0.57 | –0.29 | +0.23 | — |
| $\sigma^2$ | — | +0.20 | — | –0.14 |
| TKE | | — | — | –0.26 |

*Note:* All correlations significant at $p < 0.001$.

**TABLE 2** | Annual harmonic fit parameters for boundary layer quantities at Payerne (January 2022–December 2024, $N = 52{,}608$).

| Parameter | Amplitude | Mean | $R^2$ | Peak month |
|---|---|---|---|---|
| $\alpha$ (s–1) | 0.0063 | 0.0298 | 0.54 | January |
| $\sigma^2$ (m$^2$) | $1.9 \times 10^{-4}$ | $2.3 \times 10^{-3}$ | 0.21 | August |
| $TKE_{int}$ (m$^3$ s–2) | 23.7 | 407.9 | 0.01 | April |
| $\int w'^2 dz$ (m$^3$ s–2) | 364.7 | 1634.6 | 0.06 | February |
| Cloud (oktas) | 1.6 | 4.0 | 0.23 | January |

*Note:* All fits significant at $p < 10^{-10}$.

artifact and instead points to buoyancy-driven physics as the underlying mechanism.

### 3.3 | Annual Harmonic Analysis

To quantify the seasonal cycle objectively, we fit an annual harmonic $y(t) = A\sin(2\pi t / 365.25 + \phi) + B$ to each parameter (Table 2). The cutoff frequency $\alpha$ carries the strongest seasonal signal ($R^2 = 0.54$): the annual harmonic explains more than half the total variance and peaks in January, consistent with maximum stable stratification. The variance $\sigma^2$ peaks in August ($R^2 = 0.21$), in line with summer convective moisture enhancement. Cloud cover has a comparable seasonal component ($R^2 = 0.23$, peak January). The lidar-derived TKE displays a weaker but still statistically significant ($p < 10^{-10}$) annual component ($R^2 = 0.01$), consistent with TKE being modulated by synoptic variability on top of the seasonal cycle.

Figure 2 overlays the annual harmonic fits on the smoothed time series with monthly means. The anti-phase relationship between $\alpha$ (peak January) and $\sigma^2$ (peak August) is visually striking, with the sinusoidal fits tracking the data through three complete cycles.

Figure 3a illustrates the inverse $\alpha$–$\sigma^2$ coupling on dual axes. The seasonal anti-phase relationship persists throughout all 3 years without significant interannual variation. Figure 3b displays the positive $\sigma^2$–TKE correlation, with both parameters following seasonal convective activity.

The $\alpha$–cloud correlation ($r = +0.23$) links overcast conditions to elevated cutoff frequencies. Under cloudy skies, reduced surface heating curtails convective development, which keeps mixing shallow and turbulent structures confined.

The anisotropy index correlates negatively with TKE ($r = -0.26$), a result that is initially counterintuitive. During strong convection with high TKE, both vertical and horizontal variances increase, but horizontal components grow faster due to enhanced shear and lateral entrainment, which lowers $A$. Under stable conditions with suppressed TKE, isolated vertical motions from intermittent turbulence or gravity waves dominate over suppressed horizontal fluctuations, so $A$ rises despite low overall turbulence. The positive $A$–$\alpha$ correlation ($r = +0.20$) supports this picture: anisotropic conditions with vertical dominance exhibit higher cutoff frequencies characteristic of stable regimes.

## 4 | Discussion

### 4.1 | Physical Interpretation

The strong inverse $\alpha$–$\sigma^2$ coupling observed throughout the three-year record encodes fundamental boundary layer physics. During convective conditions driven by surface solar heating, buoyant thermals generated at the surface grow as they rise through the mixed layer, entrain environmental air, and reach the capping inversion (Kaimal et al. 1976). These ascending parcels achieve horizontal dimensions of hundreds of meters to kilometers, producing coherent turbulent motions with characteristic timescales of 10–30 min. The resulting large eddies extend the turbulent inertial range to lower frequencies (low $\alpha$) and simultaneously enhance water vapor fluctuations through vigorous vertical transport that mixes moist surface air with drier free-tropospheric air (high $\sigma^2$). The summer (JJA) coupling reaches $r = -0.82$, which identifies convection as the primary driver.

Under stable winter conditions, the physical picture differs fundamentally. Radiative cooling generates temperature inversions that suppress vertical motion. Turbulence becomes confined to shallow stable boundary layers typically less than 200–300 m deep; maximum eddy size shrinks and the spectral cutoff shifts to higher frequencies (elevated $\alpha$). Suppressed vertical mixing dramatically reduces moisture exchange and $\sigma^2$ drops. The remarkable seasonal persistence of this inverse relationship is evidence that GNSS-derived spectral parameters respond coherently to the fundamental climatological forcing of boundary layer mixing.

The dominance of vertical over horizontal velocity variance (Figure 1b) independently confirms that buoyancy-driven convection rather than mechanical shear controls $\sigma^2$ variability at Payerne. The weak meridional variance is consistent with the absence of persistent terrain-channeled flows along the Swiss Plateau and the flat topography surrounding the station.

The seasonal modulation of the $\alpha$–$\sigma^2$ coupling itself constitutes a diagnostic result. The coupling is strongest during summer (JJA: $r = -0.82$) when buoyancy-driven convection dominates both parameters simultaneously, and weakest in autumn (SON: $r = -0.12$) when frequent regime transitions between convective and stable conditions blend opposing signals within the smoothing window. The intermediate winter (DJF: $r = -0.55$) and

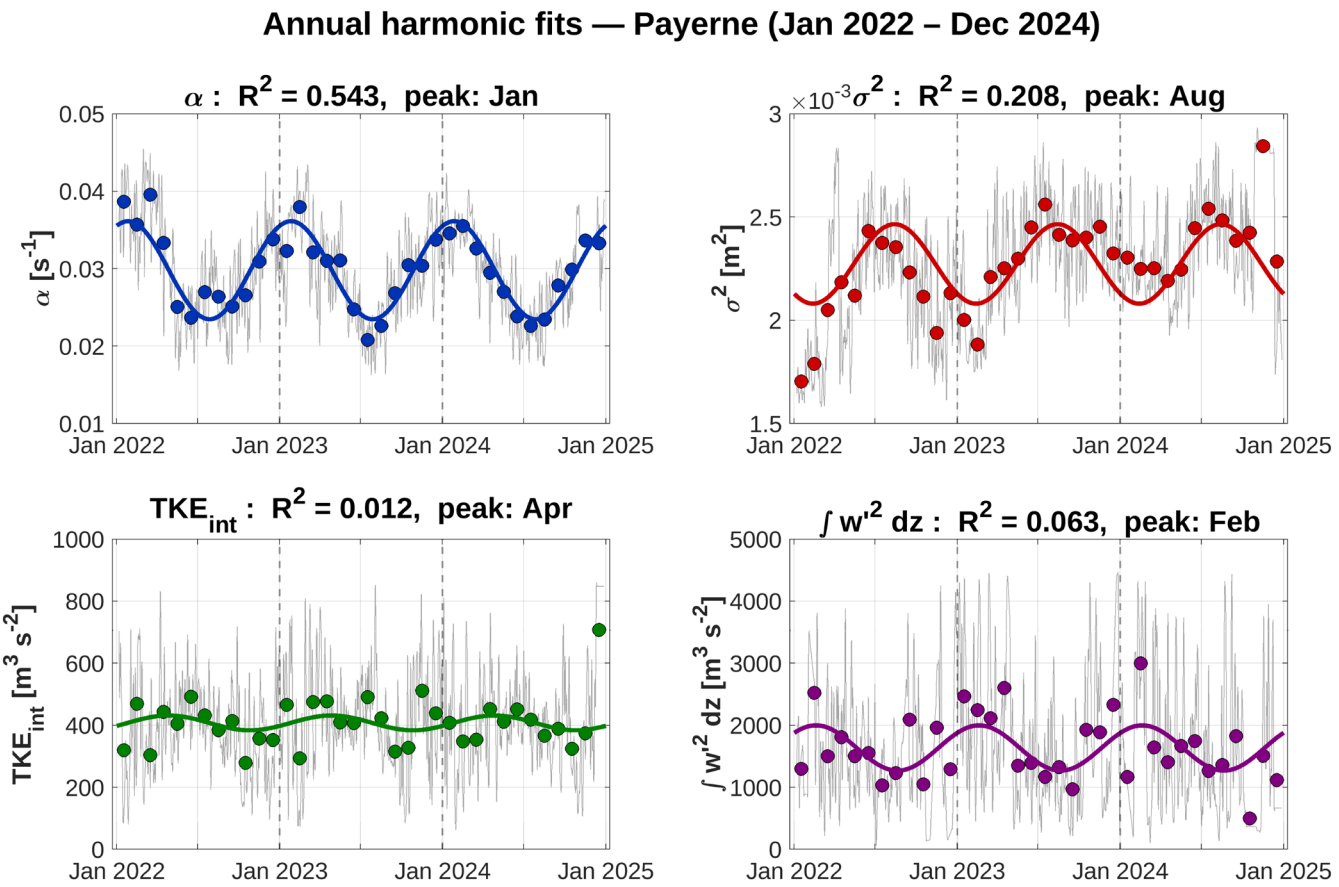


**FIGURE 2** | Annual harmonic fits (solid curves) overlaid on smoothed time series (grey) with monthly means (colored circles) for $\alpha$, $\sigma^2$, integrated TKE, and integrated vertical velocity variance. The coefficient of determination $R^2$ and peak month are indicated for each parameter. The cutoff frequency $\alpha$ carries the strongest seasonal cycle ($R^2 = 0.54$); the anti-phase between $\alpha$ and $\sigma^2$ underscores the inverse physical coupling driven by the annual modulation of convective mixing.

spring (MAM: $r = -0.40$) values correspond to progressively less uniform atmospheric forcing. This regime dependence is a prediction of the physical model: if the coupling were a statistical artifact of co-estimation, it would not vary systematically with season.

### 4.2 | Vertical Sampling Considerations

The moderate $\sigma^2$–TKE correlation ($r = +0.20$) stems from fundamental vertical sampling differences rather than weak physical connection. Lidar TKE integrates only 100–550 m and therefore captures surface-layer and lower mixed-layer turbulence but misses the entrainment zone and free troposphere. GNSS-derived $\sigma^2$ is sensitive to water vapor fluctuations along the entire tropospheric path with weighting proportional to vapor density, predominantly in the lowest 2–3 km but with contributions that extend to 5–8 km. Cloud-top radiative cooling and wind shear can also produce "upside-down" TKE profiles where turbulence peaks above mid-boundary layer, which would be partially missed by the 100–550 m integration.

Free-tropospheric moisture variability from synoptic-scale advection, frontal lifting, and upper-level dynamics contributes substantially to $\sigma^2$ without corresponding boundary layer TKE signal. This vertical sampling mismatch necessarily limits achievable correlation even when both systems respond faithfully to their respective domains. The observed $r = +0.20$ thus represents meaningful physical connection given these measurement geometry differences.

The annual harmonic analysis offers complementary validation beyond correlation magnitudes. The fact that $\alpha$ captures 54% of its variance through a single annual harmonic with physically consistent phasing (peak in January coinciding with maximum stable stratification) cannot arise from noise or instrumental artifacts. By contrast, TKE retains only $R^2 = 0.01$ for the annual harmonic, consistent with dominant control by synoptic-scale weather variability rather than the seasonal cycle alone. This asymmetry is rooted in the integrating nature of GNSS-derived parameters: ZWD, as a path-integrated quantity weighted toward the moist lower troposphere, inherently filters out local synoptic variability and retains the seasonal signal more effectively than profile-limited lidar measurements.

### 4.3 | Climatological Applications

The demonstrated three-year robustness across three complete annual cycles suggests several promising applications:

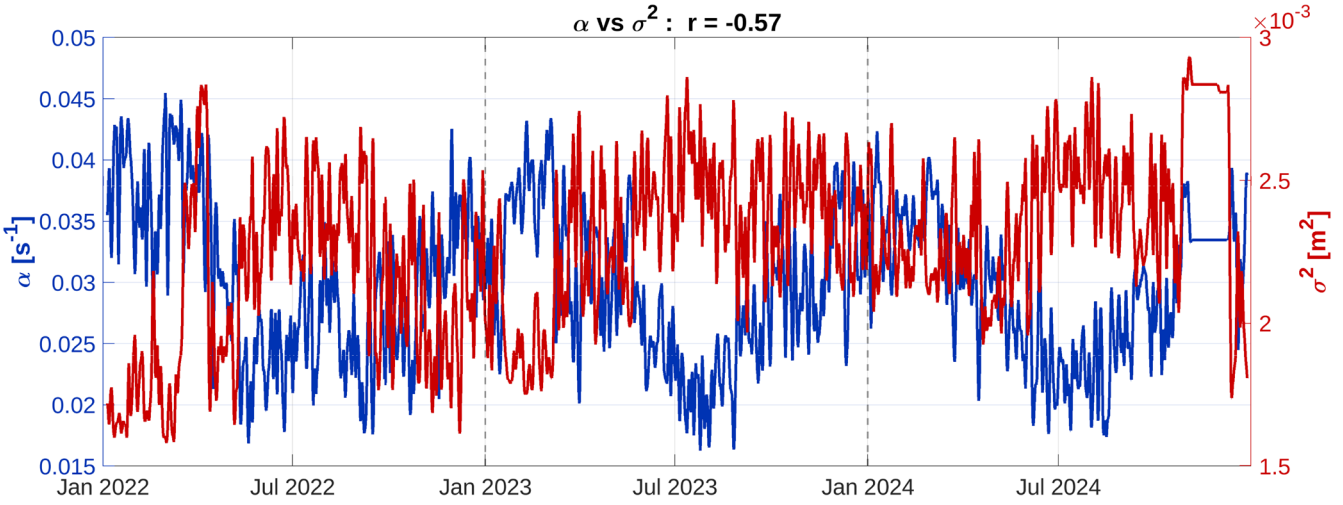


(a) Inverse coupling between cutoff frequency $\alpha$ (blue, left axis) and variance $\sigma^2$ (red, right axis), with correlation $r = -0.57$.

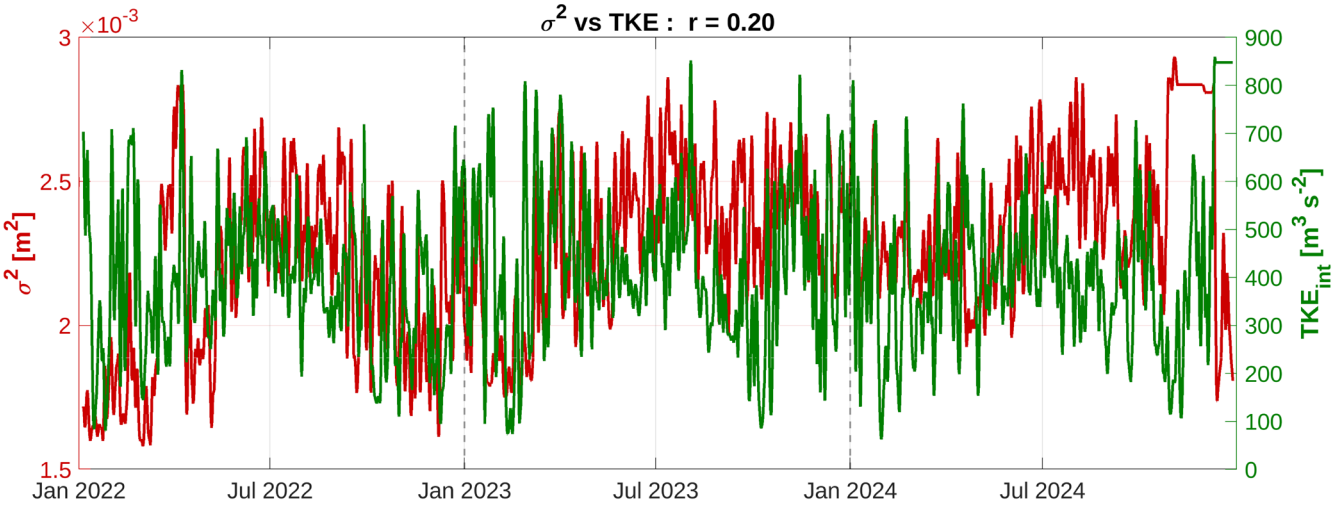


(b) Positive correlation between variance $\sigma^2$ (red, left axis) and integrated TKE (green, right axis), with correlation $r = +0.20$.

**FIGURE 3** | Dual-axis comparison of GNSS-derived and lidar-derived turbulence parameters. (a) The strong inverse $\alpha$–$\sigma^2$ relationship encodes the coupled nature of turbulence intensity and scale extent: Convective conditions produce large eddies (low $\alpha$) with enhanced moisture variance (high $\sigma^2$). (b) The positive $\sigma^2$–TKE correlation verifies that GNSS spectral variance responds to boundary layer turbulence intensity; the moderate correlation magnitude is attributable to differences in vertical sampling between the two measurement systems.

#### 4.3.1 | Boundary Layer Regime Classification

The strong $\alpha$–$\sigma^2$ coupling constitutes a two-parameter diagnostic that allows automated regime identification without ancillary measurements. Joint states with high $\sigma^2$ and low $\alpha$ mark convective conditions; elevated $\alpha$ with suppressed $\sigma^2$ signals stable stratification. This could support nowcasting of convective initiation, fog formation, and frontal passages.

#### 4.3.2 | Air Quality Monitoring

The cutoff frequency $\alpha$ varies inversely with atmospheric dispersion capacity. Elevated $\alpha$ during stable episodes corresponds to reduced vertical mixing that exacerbates pollution by trapping emissions in shallow surface layers. GNSS networks could thus deliver real-time regional surveillance of ventilation conditions.

#### 4.3.3 | Wind Energy Applications

Turbulence intensity critically affects wind turbine power variability and structural fatigue. The $\sigma^2$–TKE correlation suggests GNSS parameters could serve as proxy turbulence estimates for wind farm operations, particularly valuable for offshore locations lacking meteorological towers.

#### 4.3.4 | Climate Monitoring

Continuous GNSS archives reaching back to the mid-1990s could open the door to decadal trend analysis of boundary layer

turbulence and stability, supplying observational constraints on reanalysis products regarding convective activity changes under climate warming.

### 4.4 | Limitations

Several limitations warrant consideration. The spectral fitting assumes stationarity over 30–60 min windows, potentially violated during rapid transitions such as frontal passages or convective initiation. The Taylor frozen-flow hypothesis requires horizontal winds to substantially exceed turbulent velocities, which may fail during strongly convective or calm conditions. Because ZWD is a path-integrated measurement, altitude-specific attribution is not possible without additional profiling information. Extension to multiple sites across diverse climate zones would establish the generality of observed correlations.

## 5 | Conclusions

This study establishes the robustness of GNSS-derived boundary layer turbulence metrics through analysis of three complete years (January 2022–December 2024) of co-located GNSS and Doppler lidar observations at Payerne, Switzerland. Three principal findings emerge:

First, the cutoff frequency $\alpha$ exhibits a strong annual cycle ($R^2 = 0.54$) with the seasonal harmonic accounting for more than half of its total variance, peaking in January during maximum stable stratification. The variance $\sigma^2$ peaks in August ($R^2 = 0.21$). The inverse $\alpha$–$\sigma^2$ coupling ($r = -0.57$ over the full record, tightening to $r = -0.82$ during summer) embodies the fundamental physical relationship between turbulent scale extent and intensity. Summer convection produces large eddies (low $\alpha$) with enhanced moisture variance (high $\sigma^2$); winter stability produces the opposite. The seasonal modulation of this coupling constitutes a new, independent line of evidence that GNSS spectral parameters encode boundary layer regime information.

Second, cross-instrument correlations between GNSS-derived parameters and lidar-derived TKE ($r(\sigma^2, \mathrm{TKE}) = +0.20$; $r(\alpha, \mathrm{TKE}) = -0.29$) verify physical correspondence with direct turbulence measurements. The moderate magnitudes are consistent with the fundamental vertical sampling mismatch between path-integrated ZWD and boundary-layer-limited lidar observations.

Third, the anisotropy index derived from velocity variance ratios ($r = -0.26$ with TKE) adds complementary regime discrimination, with vertically-dominated turbulence occurring during periods of reduced total TKE as stable conditions suppress horizontal fluctuations more than vertical.

These results establish that existing GNSS infrastructure can serve as a globally distributed observing system for boundary layer dynamics monitoring. With thousands of stations operating continuously worldwide, GNSS offers spatial and temporal coverage far exceeding conventional turbulence instrumentation without requiring additional infrastructure investment.

#### Author Contributions

**Xavier Calbet:** investigation, writing – review and editing. **Zhiguo Deng:** writing – review and editing, data curation. **Gaël Kermarrec:** conceptualization, investigation, funding acquisition, writing – original draft, methodology, validation, visualization, formal analysis, supervision.

#### Acknowledgments

The authors thank MeteoSwiss for providing access to the Doppler wind lidar and ceilometer observations at the Payerne Aerological Station. ZWD retrievals were computed using the EPOS.P8 software developed at GFZ Potsdam. We gratefully acknowledge the GRUAN Lead Centre at DWD Lindenberg for maintaining the Payerne reference site infrastructure. Open Access funding enabled and organized by Projekt DEAL.

#### Funding

This research was supported by the Deutsche Forschungsgemeinschaft (DFG) under grant KE 2453/4-1 (project number 547859686).

#### Conflicts of Interest

The authors declare no conflicts of interest.

#### Data Availability Statement

The data that support the findings of this study are openly available in ZWD_TKE_CC_Wv_Payerne at https://doi.org/10.25835/do5g6qtc.

#### References

Bevis, M., S. Businger, T. A. Herring, C. Rocken, R. A. Anthes, and R. H. Ware. 1992. "GPS Meteorology: Remote Sensing of Atmospheric Water Vapor Using the Global Positioning System." *Journal of Geophysical Research* 97, no. D14: 15787–15801.

Bonin, T. A., A. Choukulkar, W. A. Brewer, et al. 2017. "Evaluation of Turbulence Measurement Techniques From a Single Doppler Lidar." *Atmospheric Measurement Techniques* 10: 3021–3039.

Emeis, S. 2008. *Surface-Based Remote Sensing of the Atmospheric Boundary Layer*. Springer.

Guerova, G., J. Jones, J. Dousa, et al. 2016. "Review of the State of the Art and Future Prospects of the Ground-Based GNSS Meteorology in Europe." *Atmospheric Measurement Techniques* 9: 5385–5406.

Kaimal, J. C., J. C. Wyngaard, D. A. Haugen, et al. 1976. "Turbulence Structure in the Convective Boundary Layer." *Journal of the Atmospheric Sciences* 33: 2152–2169.

Kermarrec, G., X. Calbet, Z. Deng, and C. Carbajal Henken. 2025. "Measurement Report: Can Zenith Wet Delay From GNSS "See" Atmospheric Turbulence? Insights From Case Studies Across Diverse Climate Zones." *Atmospheric Chemistry and Physics* 25, no. 6: 3567–3581. https://doi.org/10.5194/acp-25-3567-2025.

Leys, C., C. Ley, O. Klein, P. Bernard, and L. Licata. 2013. "Detecting Outliers: Do Not Use Standard Deviation Around the Mean, Use Absolute Deviation Around the Median." *Journal of Experimental Social Psychology* 49, no. 4: 764–766.

Lilly, J. M. 2017. "Element Analysis: A Wavelet-Based Method for Analysing Time-Localized Events in Noisy Time Series." *Proceedings of the Royal Society A* 473, no. 2200: 20160776.

Lothon, M., F. Lohou, D. Pino, et al. 2014. "The BLLAST Field Experiment: Boundary-Layer Late Afternoon and Sunset Turbulence." *Atmospheric Chemistry and Physics* 14: 10931–10960.

Navas-Guzmán, F., R. Stubi, and N. Kampfer. 2019. "An Integrated Approach Toward the Incorporation of Middle Atmospheric Water Vapor Into the GRUAN Data Processing." *Atmospheric Measurement Techniques* 12: 2093–2106.

Neumayer, K. H., Z. Deng, G. Dick, and M. Ge. 2024. "EPOS.P8: A Multi-Technique Position and Atmosphere Processor." *GPS Solutions* 28: 46.

Newman, J. F., P. M. Klein, S. Wharton, et al. 2016. "Evaluation of Three Lidar Scanning Strategies for Turbulence Measurements." *Atmospheric Measurement Techniques* 9: 1993–2013.

Savitzky, A., and M. J. E. Golay. 1964. "Smoothing and Differentiation of Data by Simplified Least Squares Procedures." *Analytical Chemistry* 36, no. 8: 1627–1639.

Stull, R. B. 1988. *An Introduction to Boundary Layer Meteorology*. Kluwer Academic Publishers.

Sykulski, A. M., S. C. Olhede, J. M. Lilly, and E. Danioux. 2019. "Lagrangian Time Series Models for Ocean Surface Drifter Trajectories." *Journal of the Royal Statistical Society, Series C* 68: 289–318.

Tatarski, V. I. 1961. *Wave Propagation in a Turbulent Medium*. McGraw-Hill.

Taylor, G. I. 1938. "The Spectrum of Turbulence." *Proceedings of the Royal Society of London, Series A* 164: 476–490.

Thomson, D. J. 1982. "Spectrum Estimation and Harmonic Analysis." *Proceedings of the IEEE* 70, no. 9: 1055–1096.

## Appendix A

### Diurnal Case Studies

To illustrate that the seasonal patterns documented in the main text reflect the aggregate of physically meaningful diurnal cycles, we present two representative case studies: a clear-sky summer day and an overcast winter day.

#### Summer (19 September 2022)

Figure A1 illustrates classical convective boundary layer development. Integrated TKE increases sharply after 08:00 and reaches maximum values by early afternoon. The GNSS-derived $\sigma^2$ tracks this evolution, rising from nocturnal minima to afternoon peaks. The cutoff frequency $\alpha$ displays inverse behavior, with early morning maxima and midday minima as the deepening mixed layer extends the inertial range to lower frequencies. The within-day $\alpha$–$\sigma^2$ correlation reaches $r < -0.8$, consistent with the physical coupling identified in the seasonal analysis. Notably, integrated vertical velocity variance ($\int w'^2 dz$) rises before the main TKE increase, which marks the onset of buoyancy-driven vertical motions ahead of the fully developed mixed layer.

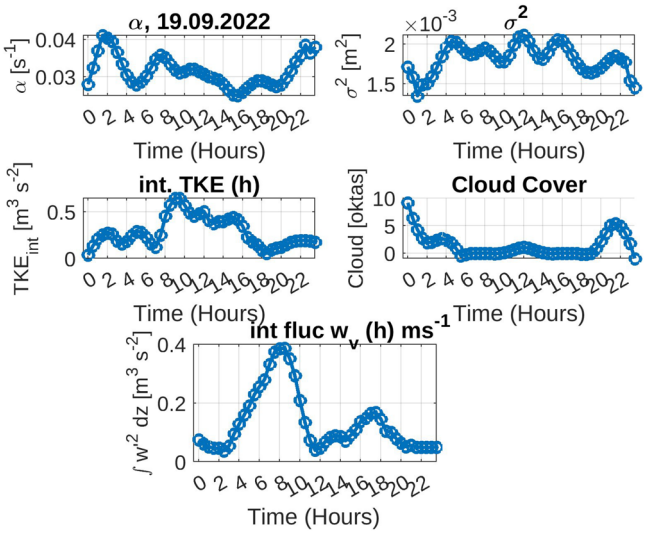


**FIGURE A1** | Diurnal evolution at Payerne on 19 September 2022 (summer). Panels display $\alpha$, $\sigma^2$, integrated TKE, cloud cover, and integrated vertical velocity variance $\int w'^2 dz$.

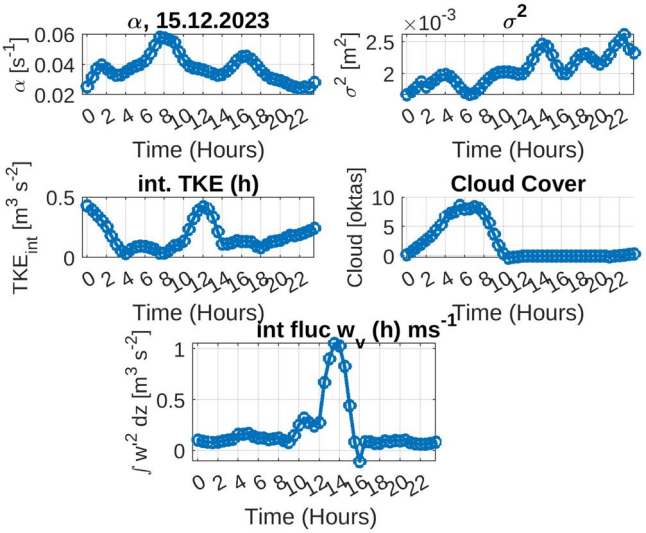


**FIGURE A2** | Diurnal evolution at Payerne on 15 December 2023 (winter). Note the reduced diurnal amplitude, quasi-periodic oscillations in $\alpha$ and $\sigma^2$ decoupled from TKE, and persistent cloud cover.

#### Winter (15 December 2023)

Figure A2 presents a contrasting case with persistent cloud cover and weak solar forcing. Integrated TKE remains low throughout the day with minimal diurnal modulation. Both $\alpha$ and $\sigma^2$ undergo quasi-periodic oscillations decoupled from TKE, which implies that ZWD fluctuations respond to advected moisture heterogeneity rather than local turbulent mixing when vertical motions are suppressed. This decoupled behavior constitutes a distinctive diagnostic signature of stable conditions, separate from the coupled inverse relationship observed during convective periods.